
Article:
Komarov, D.A., Ichikawa, Y., Yamamoto, K. et al. (7 more authors) (2018) In vivo extracellular pH mapping of tumors using electron paramagnetic resonance. Analytical Chemistry, 90 (23). pp. 13938-13945. ISSN 0003-2700

https://doi.org/10.1021/acs.analchem.8b03328

In vivo extracellular pH mapping of tumors using electron paramagnetic resonance

Denis A. Komarov,[†,¶] Yuki Ichikawa,[†] Kumiko Yamamoto,[‡] Neil J. Stewart,[†] Shingo Matsumoto,[†] Hironobu Yasui,[§] Igor A. Kirilyuk,[‖] Valery V. Khramtsov,[⊥] Osamu Inanami,[‡] Hiroshi Hirata*[†]

[†]Division of Bioengineering and Bioinformatics, Graduate School of Information Science and Technology, Hokkaido University, North 14, West 9, Kita-ku, Sapporo, 060-0814, Japan

[‡]Laboratory of Radiation Biology, Graduate School of Veterinary Medicine, Hokkaido University, North 18, West 9, Kita-ku, Sapporo, 060-0818, Japan

[§]Central Institute of Isotope Science, Hokkaido University, North 15, West 7, Kita-ku, Sapporo, 060-0815, Japan

[‖]N. N. Vorozhtsov Novosibirsk Institute of Organic Chemistry, 9, Ac. Lavrentieva Ave., Novosibirsk, 630090, Russia

[⊥]Department of Biochemistry, and In Vivo Multifunctional Magnetic Resonance center, West Virginia University, Robert C. Byrd Health Sciences Center, 1 Medical Center Drive, Morgantown, West Virginia 26506, USA

3D extracellular pH mapping; electron paramagnetic resonance; tumor microenvironment; acidification; tumor xenografts.

ABSTRACT: An electron paramagnetic resonance (EPR) based method for noninvasive three-dimensional extracellular pH mapping was developed using a pH-sensitive nitroxyl radical as an exogenous paramagnetic probe. Fast projection scanning with a constant magnetic field sweep enabled the acquisition of four-dimensional (3D spatial + 1D spectral) EPR images within 7.5 min. Three-dimensional maps of pH were reconstructed by processing the pH-dependent spectral information of the images. To demonstrate the proposed method of pH mapping, the progress of extracellular acidosis in tumor-bearing mouse legs was studied. Furthermore, extracellular pH mapping was used to visualize the spatial distribution of acidification in different tumor xenograft mouse models of human-derived pancreatic ductal adenocarcinoma cells. The proposed EPR-based pH mapping method enabled quantitative visualization of changes in extracellular pH due to altered tumor metabolism.

Glucose metabolism is altered in cancer cells,[1] and extracellular acidosis due to metabolic changes is a hallmark of tumor microenvironment.[2] Since low extracellular pH (pH_e) affects tumor progression and susceptibility to chemotherapy,[3] extracellular acidosis has received considerable attention from oncology clinicians and researchers. In light of this, accurate in vivo monitoring of pH_e is undoubtedly desirable for the study of cancer pathology and the development of new therapeutic strategies. Several methods for imaging pH in tumor tissues have been developed,[4] such as fluorescence-based pH mapping,[5] ^{31}P-nuclear magnetic resonance (NMR),[6,7] chemical exchange saturation transfer magnetic resonance imaging (CEST-MRI),[8] MRI of hyperpolarized ^{13}C-labeled bicarbonate and zymonic acid,[9,10] and proton-electron double resonance imaging (PEDRI).[11,12] However, as yet there is no gold standard for non-invasive pH_e mapping of tumors in a preclinical or clinical setting.

While electron paramagnetic resonance (EPR) has previously been used with a pH-sensitive spin probe for in vivo measurements of pH in small animals,[13–18] extension of those spectroscopic measurements to three-dimensional (3D) pH mapping in animal models using EPR is practically challenging. A major challenge of EPR-based 3D pH mapping is the longer acquisition time associated with four-dimensional (4D) EPR imaging that comprises 3D spatial and one-dimensional (1D) spectral data. Acquisition of a sufficient number of EPR spectral projections for adequate reconstruction is a critical obstacle in 3D pH mapping. Moreover, precise reconstruction of EPR spectra at the level of each voxel is essential for pH mapping with reasonable accuracy less than 0.1 pH units. This requires improvement of existing techniques for estimation of pH from EPR spectral lineshapes, in conjunction with a robust 4D image reconstruction.

In this work, we report an EPR-based method for in vivo 3D mapping of extracellular pH in mouse tumor models. This was achieved using a home-built continuous-wave (CW)-EPR imager capable of fast projection scanning,[19,20] in combination with a pH-sensitive nitroxyl probe. The probe was specifically designed for extracellular pH measurements in vivo[11] and is highly water soluble and non-toxic. The in vivo lifetime is sufficiently long (~20 min) to perform a 4D EPR acquisition. Four-dimensional EPR images were reconstructed using an optimized iterative reconstruction algorithm,[21] in conjunction with a novel procedure for the fitting of spectral data to improve reconstruction convergence to a stable solution. By this method, low-noise EPR images could be obtained even for acquired projections with a relatively low signal-to-noise ratio. We demonstrated the proposed method of 3D pH_e mapping by measuring the progress of extracellular acidosis in tumor-bearing mouse legs. Furthermore, different spatial distributions of acidification were visualized for several different tumor xenograft mouse models using human-derived pancreatic cancer cells.

EXPERIMENTAL SECTION

Chemicals. The pH-sensitive nitroxyl radical 2-(4-((2-(4-amino-4-carboxybutanamido)-3-(carboxymethylamino)-3-oxoproylthio)methyl)phenyl)-4-pyrrolidino-2,5,5-triethyl-2,5-dihydro-1H-imidazol-1-oxyl (R-SG, Fig. 1A, X = H; Y=CH_3) and its deuterium-enriched analog (dR-SG, Fig. 1A, X = D; Y=CH_3 (1/3); CD_3 (2/3)) were synthesized as previously reported.[11,12]

EPR imager. A home-built CW-EPR spectrometer/imager operating at 750 MHz was used for spectroscopy and imaging. Details of the EPR instrumentation have been reported previously.[19,20] In brief, a permanent magnet of 27 mT was used with three pairs of gradient coils and a pair of field scanning coils. A multi-coil parallel-gap resonator (22 mm diameter, 30 mm length) and a reflection-type RF bridge were used for EPR detection.[19,22]

In vitro pH mapping. The pH-sensitive nitroxyl radical R-SG, 2 mM, was dissolved in phosphate-buffered saline (PBS). Three radical solutions with pH 6.60, 6.80, and 7.00 were prepared by adding the necessary amount of HCl. The solution pH was measured using a pH meter (pH1500, Eutech Instruments, Singapore, accuracy ± 0.05 pH units) equipped with a glass electrode (InLab Semi-Micro, Mettler Toledo, Columbus, OH). The pH meter was calibrated with standard pH buffer solutions [ECBU4BT (pH=4.01), ECBU7BT (pH=7.00), and ECBU10BT (pH=10.01), Thermo Fisher Scientific, Inc., Singapore]. This calibration process ensured that the prepared radical solutions could be pH-references with the accuracy of the pH meter.

The solutions were placed into flame-sealed glass tubes with 5.3 mm inner diameter. In each case, the approximate volume of radical solution was 0.7 mL. The tubes were placed in a plastic holder made of cross-linked polystyrene, Rexolite 1422 (C-Lec Plastics Inc., Philadelphia, PA) and transferred to the resonator of the 750-MHz CW-EPR imager. The following measurement settings were used for EPR image acquisition: scan time 0.1 s, scanning magnetic field 9.0 mT, magnetic field modulation 0.2 mT, modulation frequency 90 kHz, lock-in amplifier time-constant 100 μs, number of data points 2048 per scan, and incident RF power 2.2 mW. All EPR projections were recorded with a constant sweep of the magnetic field.[21] Incrementally-ramped field gradients were used for EPR image acquisition. The projections were acquired at 15 × 15 × 15 field gradients for the X-, Y-, and Z-directions (total of 3375 projections). The maximum field gradient for each direction was 70 mT/m. The total acquisition time was 7.5 min. The pH mapping of three radical solutions was performed at room temperature (25 ºC).

In vivo pH mapping. For in vivo pH mapping of tumor-bearing mouse legs, the pH-sensitive nitroxyl radical dR-SG was dissolved in pure water (to make a concentration of 100 mM), and the solution pH was adjusted to 7.4 by the addition of NaOH. Mice were anesthetized by inhalation of 1.5–2.0% isoflurane and the tail vein was cannulated. Mice were then placed on a plastic holder made of Rexolite 1422 and transferred to the CW-EPR imager with the tumor-bearing leg positioned at the center of the resonator. The mouse body temperature and respiration rate were continuously monitored using a small animal monitoring and gating system (model 1030, SA Instruments, Inc., Stony Brook, NY). Body temperature was maintained at 36 to 37ºC by feedback-regulated heated airflow. During the EPR measurements, isoflurane anesthesia was maintained at 1.0–1.5%. The dR-SG radical (10 mg, 0.6 mmol/kg body weight) was intravenously injected as a bolus over 30 s through the tail vein catheter. Tumor model mice were weighed at 22 to 24 g at the experiments. EPR acquisition was started two minutes after the injection. The EPR settings for imaging of tumor-bearing mice were the same as those for imaging the solution samples, except for incident RF power, 11.5 mW, modulation amplitude, 0.15 mT, and lock-in amplifier time constant, 30 μs. All experiments were performed under the 'Law for The Care and Welfare of Animals in Japan' and were approved by the Animal Experiment Committee of Hokkaido University (approval no. 15-0120).

Image reconstruction and spectral data fitting. Four-dimensional spectral-spatial EPR images were reconstructed by an algebraic reconstruction technique (ART), with spectral data fitting at each iteration. All computations were performed on an Apple iMac computer (Mid 2010, Intel Core i3, 3 GHz). The reconstruction procedure was implemented in MATLAB (MathWorks, Natick, MA) with an ART algorithm written in C-language for speed and compiled as a MATLAB-executable (MEX) function. Full details of the reconstruction algorithm were reported previously.[21] 4D EPR images were reconstructed to a matrix size of 768 × 48 × 48 × 64 points, corresponding to a spectral window of 6.75 mT and field-of-view of 25 mm × 25 mm × 33.3 mm for the pH phantom, and to a matrix size of 768 × 48 × 48 × 48 points, corresponding to a spectral window of 6.75 mT and field-of-view of 25 mm × 25 mm × 25 mm for in vivo tumor-bearing mouse legs. After each ART iteration, the spatial data were smoothed

using a 3D Gaussian filter with a standard deviation of 0.8 pixels (corresponding to the full-width at half maximum (FWHM) of 1 mm). This Gaussian filter does not necessarily affect the spatial resolution when the FWHM of the Gaussian filter is sufficiently less than the spatial resolution of the mapping method that is mainly governed by the peak-to-peak linewidth of the probe and the applied magnetic field gradient.

For the fitting of spectral data, two calibration sets of EPR spectra for R-SG and dR-SG radicals were recorded over a pH range of 3 to 10, with an interval of 0.2 pH units around the pK_a value (Fig. S1). Since one of the calibration sets of EPR spectra was used for the corresponding probe in pH mapping, deuteration of the probe does not affect the hyperfine splitting and a process of pH estimation. While the hyperfine splitting structure of both probes is stable in the range of room temperature to 37 ºC, dR-SG has narrower peak-to-peak EPR absorption peaks than R-SG.[11,12,25] The spectral data of the images were fitted by a linear combination of the spectra from a corresponding calibration set. To fit the spectral data of an EPR image and generate the pH map, first, an averaged EPR spectrum for the whole sample was calculated by summing the spectral data of the image. The central line of the averaged spectrum was fitted with a Voigt profile to calculate its position on the spectral coordinate. Note, the central line of the R-SG and dR-SG spectra does not change with pH, and its position solely depends on the loading of the EPR resonator and the spectrometer settings. Using the calculated position of the central EPR line, the spectra from the calibration set (Fig. S1) were shifted to the correct field position by multiplication with a corresponding phase multiplier in the Fourier domain:

$$\mathrm{DFT}\left[\boldsymbol{B}_i(H+\ H)\right]=e^{\ 2\ i\ H}\ \mathrm{DFT}\left[\boldsymbol{B}_i(H)\right],\quad (1)$$

where DFT is the discrete Fourier transform, i is a spectrum from the calibration set, H is the magnetic field, ΔH is the difference in the magnetic field for the averaged image spectrum and the spectra from the calibration set, ξ is the Fourier domain frequency variable.

Then, for each voxel of the 4D EPR image, the spectrum from the calibration set, $\mathbf{B}_i$ which best describes the observed spectrum, **E**, was determined by solving the equation for the linear coefficient, c_i, and finding the minimum of the residual sum of squares, RSS, defined as follows:

$$c_i=\frac{\boldsymbol{B}_i\times\boldsymbol{E}}{\boldsymbol{B}_i\times\boldsymbol{B}_i},\quad (2)$$

$$RSS=\left\|\boldsymbol{E}\quad c_i\boldsymbol{B}_i\right\|.\quad (3)$$

After finding the closest-matching spectrum $\mathbf{B}_i$, the observed spectrum, **E**, was fitted by the linear combination of $\mathbf{B}_i$ and its two neighboring spectra, with a non-negative constraint:

$$\boldsymbol{E}\quad a_{i\ 1}\boldsymbol{B}_{i\ 1}+a_i\boldsymbol{B}_i+a_{i+1}\boldsymbol{B}_{i+1}.\quad (4)$$

Finally, the pH value of the voxel was calculated according to the formula:

$$\mathrm{pH}=\mathrm{pK_a}+\log_{10}\frac{\sum a_i\left[R\right]_i}{\sum a_i\left[RH^+\right]_i},\quad (5)$$

where $[RH^+]_i$ and $[R]_i$ are the known concentrations of protonated and unprotonated forms of the radical for each particular calibration solution. The pK_a for the R-SG and dR-SG radical was 6.84 at 23 ºC and 6.60 at 37 ºC.[11] Since in vitro pH mapping was performed at room temperature (25 ºC), we set pK_a at 6.80 pH units. Since the evidence in which the temperature does not affect the hyperfine splitting constants of R-SG and dR-SG was previously reported,[11,12,25] we did not take a shift in the hyperfine splitting constants into account for different temperatures in our study.

In this approach, the method for solving the linear equations (eq. 4) was employed to obtain the approximation of the whole spectral line-shape at each voxel. Our method is close to the concept of the matching pursuit algorithm for obtaining an approximation of the whole spectral line-shape. While an apparent hyperfine splitting constant for three-line EPR absorption peaks was measured to determine pH values in our previously reported work,[23] it was no longer applied to pH measurements in this study.

Functional resolution and trueness. For solution samples, functional resolution of pH measurements was defined as the full-width at half maximum (FWHM) of the normal curve that reflects the probability density of pH values at each voxel:

$$\mathrm{FWHM}=2SD\sqrt{2\log_e 2}=2.35SD,\quad (6)$$

where SD is the standard deviation of measured pH values at each voxel and e is Napier's constant. In this estimation, we assumed the normal distribution for pH values at each voxel. After computing SDs of pH values in each solution contained in three tubes, FWHMs were obtained for corresponding solutions. In our experiments, we defined the functional resolution of pH measurements as the mean of three FWHMs. This functional resolution corresponds to "precision" that is defined as the closeness of agreement between pH values at each voxel. Moreover, the trueness of pH measurements was defined as the closeness of agreement between the average value obtained from pH values at each voxel and a reference value, which is a known pH value of a sample solution in our case. This trueness is generally called "accuracy" in common technical definition. In this study, we defined the trueness of pH measurements for three samples as the mean of the differences between the average pH values of each tube obtained by EPR-based pH mapping and the reference pH values (6.60, 6.80, and 7.00 pH units) measured by a commercial pH meter mentioned above.

Magnetic resonance imaging. MRI was performed on a home-built 1.5 T permanent magnet system, using a home-built ^{1}H mouse body coil and a dedicated spectrometer (MR Solutions, Guildford, UK). The same mouse bed was used for both EPR and MRI to ensure approximately equivalent scan positioning and facilitate image registration. A 2D T_2-weighted fast spin echo sequence was used for anatomical imaging of the tumor-bearing leg. Sequence parameters were as follows: field-of-view (FOV) 32 mm × 32 mm; 128 × 128 in-plane matrix; 32 slices of thickness 2 mm, overlap 1mm; echo/repetition time (TE/TR) 68/4876 ms; echo train 8; number of averages 3; scan time ~4 min. 2D scans were acquired in all three anatomical planes to permit reconstruction of arbitrary slices for accurate spatial comparison with the 3D EPR imaging data. Tumor volume was evaluated from MRI by selecting the tumor region on sagittal-plane images.

Statistical analysis. To compare the mean values of the median pH_e of tumor-bearing mice, a two-tailed paired t-test was used. The sample size of tumor-bearing mice (n = 7) was selected based on previously reported pH_e data of SCC VII tumor-bearing mice,[23] in which the change in the mean pH_e for the tumor-bearing legs between day 5 and 8 was 0.12 pH units and the standard deviation of a single pH measurement was 0.076 pH units. Using these values and choosing the level of Type I error α = 0.05 and Type II error β = 0.2 for pH measurements yielded a required sample size of 7.[24] For the animal study of pH_e mapping during tumor growth, randomization was not used and no blinding was done because of the paired nature of the experiment.

RESULTS

3D pH mapping calibration with solution samples. We used an imidazoline nitroxyl radical bound with glutathione (R-SG, see Fig. 1a for the structure) as a spin probe for pH measure-

ments by EPR.[11,25,26] This radical probe shows a pH-dependent EPR spectrum with different hyperfine splitting constants for protonated and unprotonated forms as shown in Fig. 1b (also see Supporting Information Fig. S1 for EPR spectra at various pH values). The pK_a value of the radical is 6.6 at 37 °C which is suitable for pH measurements in the normal physiological range and slightly acidic conditions.

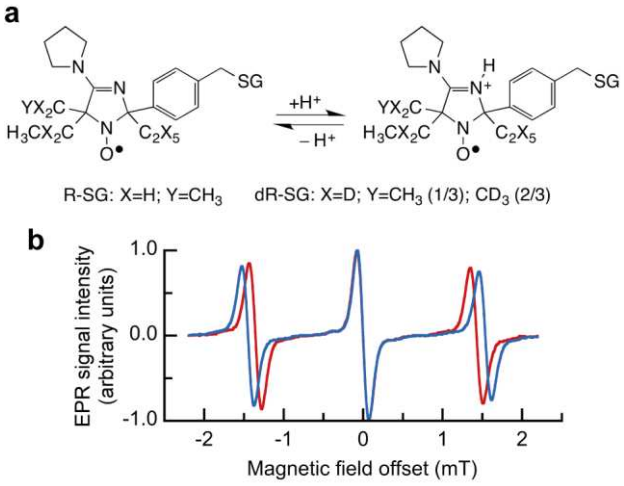

Figure 1. pH-sensitive radical probe and its EPR spectra. (a) Chemical structures and scheme of protonation of pH-sensitive nitroxyl radical (R-SG) and its deuterium-enriched analog (dR-SG). (b) First-derivative EPR spectra of 2 mM dR-SG measured at 750 MHz in alkaline (pH = 10, blue line) and acidic (pH = 3, red line) solutions. SG stands for glutathione residue. Note, the central line of the spectra does not depend on pH.

The proposed method of 3D pH mapping was experimentally verified using a solution phantom consisting of three glass tubes with 2 mM R-SG solutions at pH 6.6, 6.8, and 7.0. Fig. 2a shows a photograph of the phantom. We performed 4D EPR imaging with a total data acquisition time of 7.5 min. After image reconstruction and spectral data fitting, 3D maps of EPR signal intensity and pH were obtained. Fig. 2b shows a surface-rendered image of the EPR signal distribution that accurately reflects the geometry of the solution phantom. Figs. 2c and 2d show corresponding maps of the EPR signal intensity and pH for the cross-sectional slice shown at the center of Fig. 2b, respectively. Fig. 2e shows the histograms of pH values for each of the three tubes. The measured pH values were 6.591 ± 0.025, 6.839 ± 0.035 and 7.029 ± 0.039 (mean ± standard deviation), which well reproduced the real pH values. Here the standard error of the mean for a solution (7.00 pH units) was 0.0006, because of sample size n = 4923 (voxels). Therefore we expressed the mean and the standard deviation of pH values to three decimal places. From the calculated standard deviations above, functional resolution (also called precision) of pH measurements was estimated to be 0.078 pH units according to its definition in the Experimental Section. The trueness of pH measurements was also estimated to be 0.026 pH units. This trueness (accuracy) was within the precision of a commercial pH-meter we used.

Using a phantom with three solution samples (Fig. 2), we demonstrated the capability of spectral-spatial EPR imaging for 3D spatially-resolved pH measurements with a functional resolution of about 0.078 pH units. By fitting the signal distributions in Fig. 2c with a Gaussian function, the spatial resolution of pH maps was determined as 3 mm. In practice, the spatial resolution of an EPR imaging experiment depends on the width of the spectral line and the applied magnetic field gradient. The gradient is typically limited by the signal-to-noise ratio of acquired EPR projections. In our case, the maximum gradient of the magnetic field was 70 mT/m, and the peak-to-peak linewidth of the R-SG probe was 0.21 mT. Thus, the spatial resolution can be estimated as linewidth/gradient = 3 mm, which accurately repeats the Gaussian fitting result given above.

Extracellular acidosis during tumor growth. In vivo EPR-based pH mapping was demonstrated using tumor-bearing mice. The progress of acidification in murine squamous cell carcinoma (SCC VII) cells implanted into the right hind legs of mice was monitored. (Full details of animal preparation are

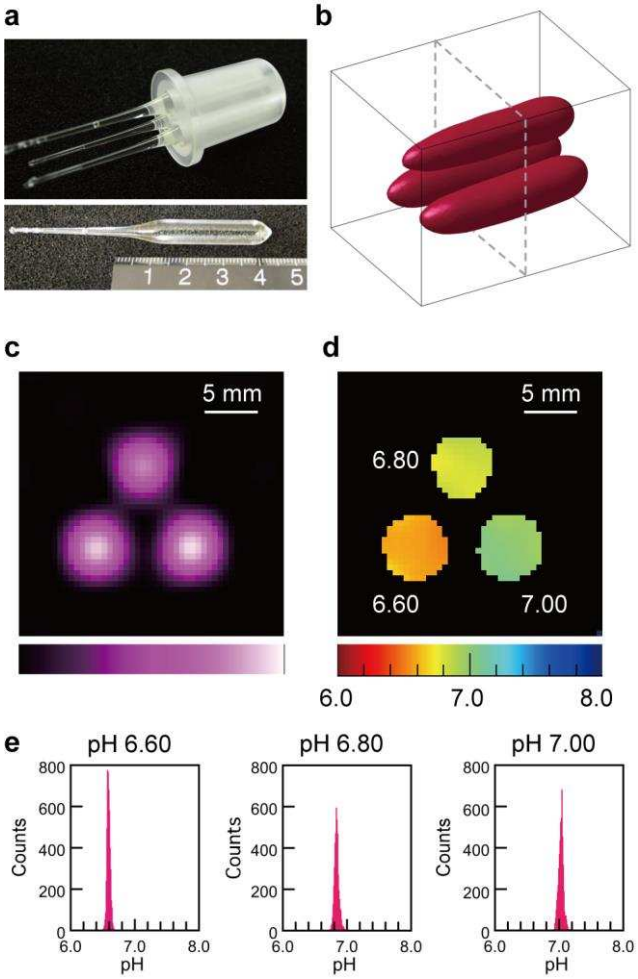

Figure 2. Three-dimensional visualization and EPR characterization of a pH phantom. (a) Photograph of the phantom sample, consisting of three flame-sealed glass tubes (inner diameter 5.3 mm, volume ~0.7 mL) placed in a plastic holder (Scale in cm). The tubes were filled with 2 mM solutions of R-SG in PBS with pH values adjusted to 6.60, 6.80, and 7.00. (b) 3D surface-rendered image of EPR signal intensity calculated with a 35% threshold: image matrix size 48 × 48 × 64, field-of-view 25.0 mm × 25.0 mm × 33.3 mm. (c) EPR signal intensity distribution, and (d) map of pH for the central slice of the 3D image (indicated by dashed lines in (b)), shown with a 35% threshold of signal intensity and pH, respectively. (e) Histograms of pH for each of the three tubes. The measured pH values were 6.591 ± 0.025, 6.839 ± 0.035 and 7.029 ± 0.039 (mean ± standard deviation).

given in Supporting Information.) To increase the sensitivity of EPR measurements and achieve a better spatial resolution, the deuterated radical dR-SG (Fig. 1a) was used for in vivo pH mapping. The deuterated radical dR-SG has an EPR linewidth of about 0.12 mT. However, the projections were recorded with a modulation amplitude of 0.15 mT (rather than 0.2 mT) to achieve a better signal-to-noise ratio. Therefore, we estimate that the spatial resolution of the in vivo measurements was ~2 mm. In addition, an in vitro cytotoxicity test for R-SG (see Supporting Information, Fig. S2) showed that 56% of HeLa cells survived when incubated with 10 mM R-SG for 4 days.

Fig. 3a shows a photograph of the leg of an SCC VII tumor-bearing mouse placed on a plastic holder for EPR measurements. The dashed lines indicate the region visualized by EPR imaging. Fig. 3b shows surface-rendered EPR images of the leg (and part of the tail) of a mouse measured at 5 and 8 days after tumor implantation. Figs. 3c and 3d show T_2-weighted anatomical MR images for the sagittal plane on day 5 and 8, respectively. The corresponding maps of the EPR signal intensity are given in Figs. 3e and 3f. The positions of the maps are shown in Fig. 3b with dashed lines. Both MR and EPR images demonstrated enlargement of the tumor over time. Also, the EPR images revealed a low-signal-intensity area in the center of the tumor that presumably appeared due to insufficient delivery of the spin probe to the relatively poorly perfused tumor tissue. The size of the low-intensity area significantly increased on day 8 compared with day 5.

Extracellular pH was visualized for the tumor-bearing leg in 3D. Figs. 3g (day 5) and 3h (day 8) present the maps of pH_e in the sagittal plane corresponding to the EPR signal intensity maps in Figs. 3e and 3f. Masks generated from MR anatomical images were applied to remove pH data outside the leg. The maps of pH_e obtained on day 5 revealed some regions in which pH decreased to approximately 6.6, while most of the leg had pH above 7.0. Regions of acidosis became significantly larger on day 8. To quantitatively characterize the change in tumor acidification, a 3D region of interest (ROI) that included the whole thigh muscle and the tumor graft was defined by selecting ROIs in all 2D slices of sagittal MR images (red lines in Figs. 3c, 3d.

Quantitative analysis of pH_e data is presented in Figs. 3i to 3l. Fig. 3i shows the representative histograms of pH_e data for the mouse shown in Fig. 3. The overlaid histograms show that the distribution of pH_e was slightly shifted to lower pH on day 8. To confirm the reduction in pH_e of SCC VII tumors, we measured seven tumor-bearing mice in total on day 5 and 8. The tumor volumes, median pH_e values and acidic tumor volumes (pH_e < 7.0) for seven mice are summarized in Figs. 3j to 3l. The mean tumor volumes on day 5 and 8 were 0.70 cm^3 and 0.97 cm^3, respectively (two-tailed paired t-test, P = 0.002, n=7). The means of the median pH_e on day 5 and 8 were 7.11 and 7.04, respectively (two-tailed paired t-test, P = 0.025, n=7). Moreover, the means of acidic tumor volumes (pH_e < 7.0) on day 5 and 8 were 0.14 cm^3 and 0.38 cm^3, respectively (two-tailed paired t-test, P=0.007, n=7).

Three-dimensional pH mapping was successfully performed within 7.5 min for a living mouse using a single bolus injection of dR-SG, as shown in Fig. 3. EPR signal kinetics of the R-SG spin probe measured in vivo in mouse tumors on day 5 and 8 after implantation of SCC VII cells are provided in Supporting Information (Fig. S3). On both occasions, the EPR signal kinetics were comparable; signal appeared immediately after the intravenous injection of the probe, reached a maximum after about 2 minutes and then gradually declined. The intensity of EPR signal was approximately 80% of its maximum 10 minutes after probe injection (Fig. S3). The 4D spectral-spatial EPR imaging acquisition was thus designed to acquire 3375 projections between 2 and 9.5 minutes post injection of the probe. The primary route of radical removal from the animal is likely its reduction to the corresponding hydroxylamine, followed by renal excretion. Supporting this hypothesis, a high concentration of the reduced form of dR-SG was detected in the mouse urine after the experiments (see Fig. S4). The dependence of the measured pH_e value on the signal intensity is provided in Supporting Information (Fig. S5). The relation between the signal intensity and pH_e in the 3D data had no correlation.

pH mapping of tumor xenograft mouse models. The proposed method of 3D pH_e mapping for detection of extracellular acidosis was further validated using three types of tumor xenograft mouse models. We used the human-derived pancreatic ductal adenocarcinoma cells MIA PaCa-2, SU.86.86, and Hs766t. (Full details of animal preparation are given in Supporting Information.) It was previously shown that these tumor types exhibit different levels of oxygenation and pyruvate metabolism by EPR and hyperpolarized ^{13}C MRI.[27] Fig. 4a shows sagittal T_2-weighted MR anatomical images of tumor-bearing mouse legs with MIA PaCa-2, SU.86.86, and Hs766t tumor xenografts. All three tumors were similar in size on the day of the measurements; ROI volumes were 1.09, 1.11, and 0.99 cm^3 for MIA PaCa-2, SU.86.86, and Hs766t tumors, respectively. Corresponding maps of the EPR signal intensity and pH_e are shown in Figs. 4b and 4c. For the MIA PaCa-2 tumor xenograft, the EPR signal intensity was relatively homogeneous, indicating a uniform distribution of the spin probe inside the tumor. The observed pH_e in all regions of the tumor was above 6.8. In contrast, the SU.86.86 tumor xenograft exhibited a large area of low or no EPR signal, making it impossible to calculate pH at the center of the tumor (void area in pH_e map, Fig. 4c). Severe extracellular acidosis (pH_e 6.2–6.3) was observed in other regions of the tumor. For the Hs766t tumor, some areas of low EPR signal intensity were also observed (pH_e 6.5–6.6). Notably, the areas with low pH_e did not directly correlate with the EPR signal intensity, i.e., spin probe concentration, in this tumor type. In total, three mice bearing

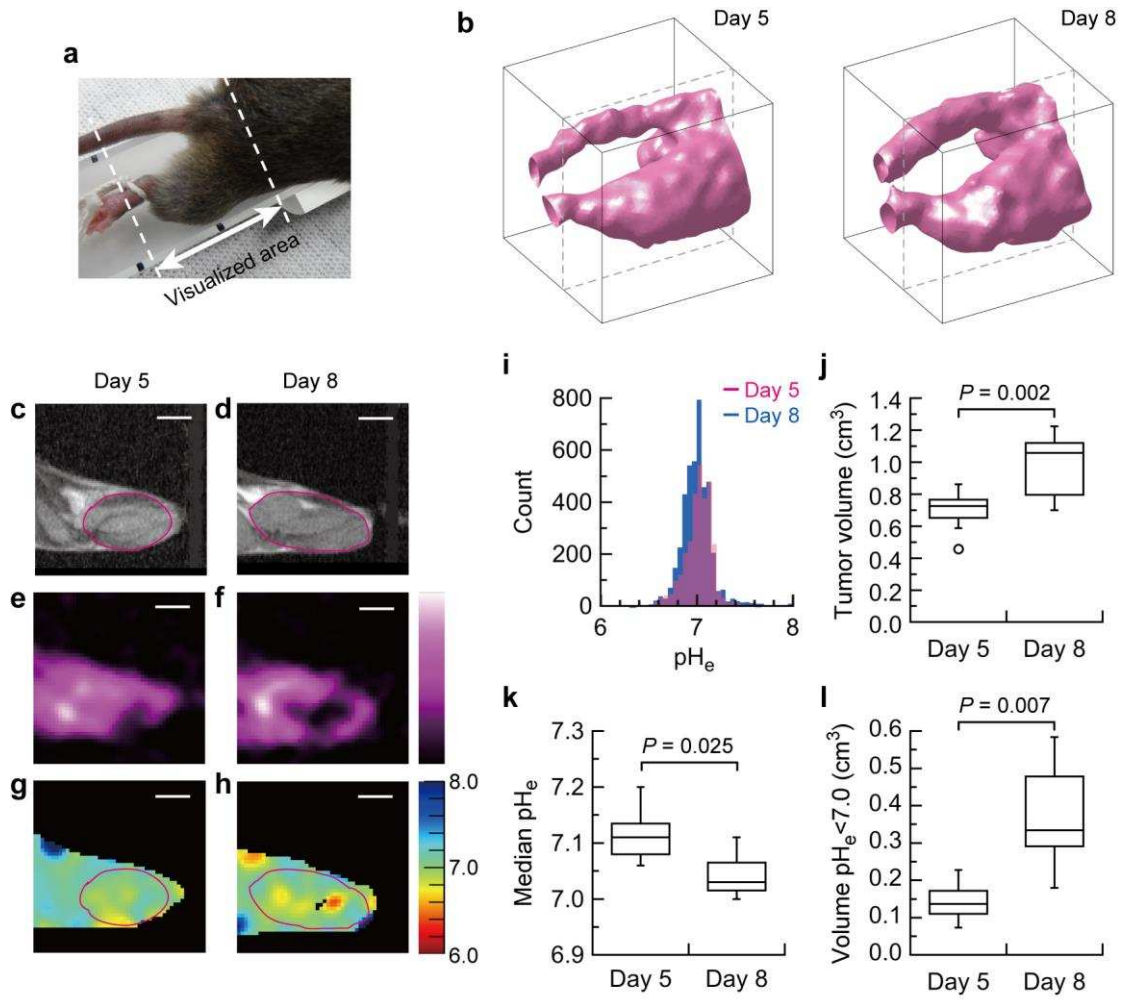

Figure 3. Progress of acidification in an SCC VII tumor-bearing mouse leg during tumor growth. (a) Photograph of the mouse leg fixed on a plastic holder and (b) 3D surface-rendered images of EPR signal measured at day 5 and day 8 after tumor implantation. The image matrix size was 48 × 48 × 48, field-of-view 25.0 mm × 25.0 mm × 25.0 mm. (c) and (d) T_2-weighted proton MR anatomical images of the mouse leg in the sagittal plane, acquired at day 5 and 8, respectively, scaled and cropped to match the EPR images. (e, f) Representative slices of EPR signal intensity taken from the 3D data, and (g, h) corresponding maps of pH_e. The white scale bar on the images corresponds to 5 mm. (i) Representative histograms of voxel-wise pH_e data measured on day 5 (red) and 8 (blue) for a single mouse. Box-and-whisker plots of (j) the tumor volume, (k) the median pH_e, and (l) the acidic tumor volume (pH_e < 7.0) for n = 7 mice. The circle in Fig. 4j represents an outlier. A two-tailed paired t-test was used to determine statistical significance P.

MIA PaCa-2, two mice bearing SU.86.86, and two mice bearing Hs766t tumors were scanned. In all cases, results similar to those presented in Fig. 4 were obtained. The mean values of the median pH_e were 7.05 (MIA PaCa-2, n=3), 6.90 (SU.86.86, n=2), and 6.91 (Hs766t, n=2).

DISCUSSION

The functional resolution of pH is an essential aspect of our method of pH mapping. Since the probe loses the sensitivity to pH at a pH value far from pK_a, the trueness and the functional resolution of pH measurements depend on the pH value being measured. This sensitivity dependence in pH measurements using R-SG was previously reported.[23,25] However, our EPR-based pH mapping can provide its best pH resolution around pK_a due to the characteristics of R-SG and dR-SG. Since pK_a of R-SG at 37 ºC is 6.60 pH units, this probe can cover the biologically relevant range of pH_e in normal tissues (close to 7.4 pH units) and in acidic condition (below 7.0 pH units and even close to 6.0 pH units).

The transient increase in the concentration of the radical in the blood during EPR acquisitions should not have any significant harmful effect on the animal. For in vivo 3D pH mapping, we used a rather high dosage of the spin probe (10 mg or 0.6 mmol/kg body weight) injected intravenously. Assuming that mouse blood volume is approximately 1.5 mL, the peak concentration of the radical in the blood could reach ~10 mM.

Using EPR imaging, we were able to generate 3D maps of extracellular pH and visualize the expansion of regions of acidosis with tumor development (Fig. 3). Murine squamous cell carcinoma SCC VII is a well-documented fast-growing tumor,[28] and is known to exhibit some regions of severe hypoxia and localized alterations in cellular glucose metabolism.[29] In previous EPR (1D) spectroscopy measurements, it was shown that the average pH_e of SCC VII tumors gradually decreased over 11 days post-implantation.[23] However, the spatial distribution of pH_e in tumors cannot be visualized by spectroscopic measurements. In all measured tumors, we observed a region of low EPR signal intensity. However, the T_2-weighted MR

anatomical images revealed no clear structural peculiarities in the corresponding region (see Figs. 3d and 3f). Considering the intravenous route of dR-SG administration, the low EPR signal most likely indicates necrotic regions inside the tumor, as well as low vascular delivery, which may be due to a combination of necrosis, low angiogenesis, interstitial pressure, or other conditions.

The temperature dependence of pK_a is 0.017 pH units/ºC that is calculated from the reported pK_a values at 23 and 37 ºC. This dependence is well below our functional resolution of pH measurements (0.078 pH units). Therefore a little change in body temperature during image scanning does not significantly affect our results of pH mapping.

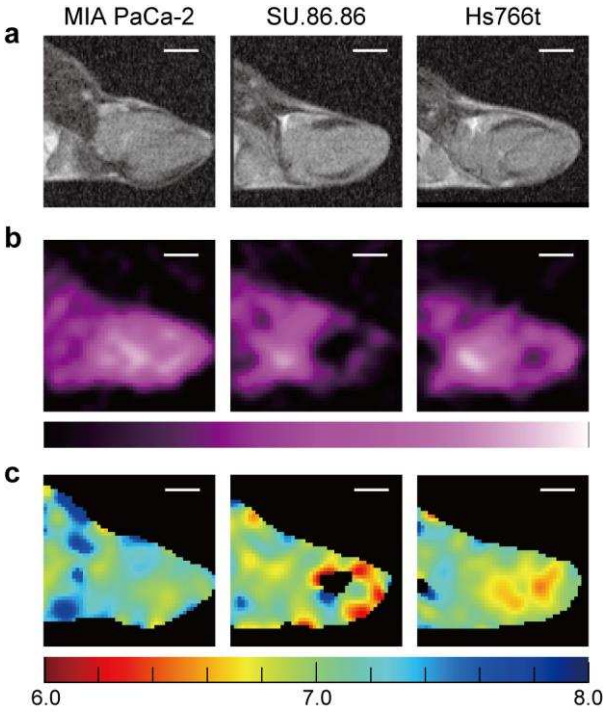

Figure 4. Visualization of pH_e in mouse legs bearing the human-derived pancreatic ductal adenocarcinoma xenografts MIA PaCa-2, SU.86.86, and Hs766t. (a) Representative T_2-weighted MR anatomical images of tumor-bearing mouse legs in the sagittal plane, (b) corresponding slices of EPR signal intensity, and (c) maps of pH_e. The matrix size of the EPR images was 48 × 48 × 48, field-of-view 25.0 mm × 25.0 mm × 25.0 mm. MR images were scaled and cropped to match the corresponding EPR images. The white scale bar on the images corresponds to 5 mm.

In addition to the temperature dependence, a probe concentration in extracellular space in tumors may have an impact on the resultant pH_e values. For the accurate pH_e measurements, it is essential to keep the probe concentration below the buffer capacity of the blood. To clarify this influence, the concentration of dR-SG in extracellular space should be quantitatively identified. This problem requires further consideration of kinetics and spatial distribution of the probe in a subject mouse as well as experimental verification of the extracellular probe concentration.

No direct correlation between the signal intensity and pH_e was observed (Fig. S5). The observed areas of extracellular acidosis were frequently located near the borders of weakly perfused tissue. This acidosis may be explained by the fact that tissue near the tumor periphery likely has better access to metabolic nutrients and thus a higher rate of glycolysis, while the cells deep inside the tumor may remain dormant. Interestingly, acidic pH_e near the tumor peripheries was previously observed for rat gliomas measured by an MR spectroscopic imaging technique.[30]

Our proposed EPR imaging method for pH_e mapping also enabled the visualization of differences in extracellular acidosis for three types of human-derived pancreatic ductal adenocarcinoma xenografts. The human-derived cancer cells MIA PaCa-2, SU.86.86, and Hs766t were previously studied for glucose metabolism and oxygenation.[27] It was reported that the SU.86.86 tumor xenograft has high vascular density and a lower rate of pyruvate to lactate metabolic conversion in vivo than MIA PaCa-2 or Hs766t tumors.[27] In contrast, in our measurements, a very low EPR signal was detected inside the SU.86.86 tumor. Because the spin probe was injected intravenously and EPR measurements were performed within 10 minutes of injection, we believe that the EPR signal intensity distribution reflects how well the tumor tissue is perfused by the blood. In this context, the obtained data suggest that SU.86.86 has relatively low blood supply. Furthermore, the SU.86.86 tumor demonstrated the strongest acidosis among all tumor xenografts. Some regions of low signal intensity and pronounced acidosis were also detected in the Hs766t tumor. In contrast, MIA PaCa-2 showed relatively high EPR signal throughout the whole tumor and exhibited only mild extracellular acidosis. According to reference,[27] the tumor cells of both MIA PaCa-2 and Hs766t have a high rate of proton production in vitro and rapidly convert pyruvate to lactate in vivo. Thus, the milder acidosis of MIA PaCa-2 tumors observed by EPR imaging in this study may be attributed to better perfusion of the tumor, faster proton removal by the blood and possibly more efficient mitochondrial respiration.

CONCLUSION

We demonstrated a method for EPR-based in vivo pH mapping of mouse tumors. The method is capable to quantitatively visualize the progress of tissue acidification during tumor growth and to distinguish different levels of extracellular acidosis in various tumor models. Monitoring of extracellular pH in vivo may offer a powerful tumor assessment tool for a variety of preclinical studies, in order to establish the metabolic profile of novel cancer tumor models and to develop new therapeutic strategies.

ASSOCIATED CONTENT

Supporting Information

The Supporting Information is available free of charge on the ACS Publications website.

Experimental details of cytotoxicity assay, animal preparation and tumor models, and Figures S1–S4 (PDF).

AUTHOR INFORMATION

Corresponding Author

* hhirata@ist.hokudai.ac.jp

ORCID

Valery V. Khramtsov: 0000-0001-6187-5546
Osamu Inanami: 0000-0001-7895-3918

Hiroshi Hirata: 0000-0002-6906-1608

Present Address

¶ D.A.K.: Davis Heart and Lung Research Institute, The Ohio State University, Columbus, Ohio 43210, USA.

Author Contributions

The manuscript was written through contributions of all authors. All authors have given approval to the final version of the manuscript.

Notes

The authors declare no competing financial interest.

ACKNOWLEDGMENT

This work was supported in part by Japan Society for the Promotion of Science (JSPS) KAKENHI Grant number 26249057 (to H.H.), Japan Science and Technology Agency (JST)-PRESTO (to S.M.), Ministry of Education and Science of the Russian Federation, application no. 2017-220-06-7355 (to I.A.K.), and National Institutes of Health (NIH) Grants CA194013 and CA192064 (to V.V.K.). N.J.S. is a JSPS International Research Fellow.

REFERENCES

(1) Denko, N. C. Hypoxia, HIF1 and glucose metabolism in the solid tumour. Nat. Rev. Cancer **2008**, 8, 705–713.

(2) Swietach, P.; Vaughan-Jones, R. D.; Harris, A. L.; Hulikova, A. The chemistry, physiology, and pathology of pH in cancer. Phil. Trans. R. Soc. B **2014**, 396, 20130099.

(3) Corbet, C.; Feron, O. Tumour acidosis: from the passenger to the driver's seat. Nat. Rev. Cancer **2017**, 17, 577–593.

(4) Zhang, X.; Kin, Y.; Gillies, R. J. Tumor pH and its measurement. J. Nucl. Med. **2010**, 51, 1167–1170.

(5) Helmlinger, G.; Yuan, F.; Dellian, M.; Jain, R. K. Interstitial pH and pO_2 gradients in solid tumors in vivo: High-resolution measurements reveal a lack of correlation. Nat. Med. **1997**, 3, 177–182.

(6) Gillies, R. J.; Liu, Z.; Bhujwalla, Z. ^{31}P-MRS measurements of extracellular pH of tumors using 3-aminopropylphosphonate. Am. J. Physiol. Cell. Physiol. **1994**, 267, C195–C203.

(7) Schmid, A. I.; Meyerspeer, M.; Robinson, S. D.; Goluch, S.; Wolzt, M.; Fiedler, G. B.; Bogner, W.; Laistler, E.; Kršňák, M.; Moser, E.; Trattnig, S.; Valkovič, L. Dynamic PCr and pH imaging of human calf muscles during exercise and recovery using ^{31}P gradient-Echo MRI at 7 Tesla. Magn. Reson. Med. **2016**, 75, 2324–2331.

(8) Chen, L. Q.; Randtke, E. A.; Jones, K. M.; Moon, B. F.; Howison, C. M.; Pagel, M. D. Evaluations of Tumor Acidosis Within In Vivo Tumor Models Using Parametric Maps Generated with AcidoCEST MRI. Mol. Imaging. Biol. **2015**, 17, 488–496.

(9) Gallagher, F. A.; Kettunen, M. I.; Day, S. E.; Hu, D. E.; Ardenkjær-Larsen, J. H.; Zandt, R. i.; Jensen, P. R.; Karlsson, M.; Golman, K.; Lerche, M. H.; Brindle, K. M. Magnetic resonance imaging of pH in vivo using hyperpolarized ^{13}C-labelled bicarbonate. Nature **2008**, 453, 940–943.

(10) Düwel, S.; Hundshammer, C.; Gersch, M.; Feuerecker, B.; Steiger, K.; Buck, A.; Walch, A.; Haase, A.; Glaser, S. J.; Schwaiger, M.; Schilling, F. Imaging of pH in vivo using hyperpolarized ^{13}C-labelled zymonic acid. Nat. Commun. **2017**, 8, 15126.

(11) Bobko, A. A.; Eubank, T. D.; Voorhees, J. L.; Efimova, O. V.; Kirilyuk, I. A.; Petryakov, S.; Trofimiov, D. G.; Marsh, C. B.; Zweier, J. L.; Grigor'ev, I. A.; Samouilov, A.; Khramtsov, V. V. In Vivo Monitoring of pH, redox status, and glutathione using L-band EPR for assessment of therapeutic effectiveness in solid tumors. Magn. Reson. Med. **2012**, 67, 1827–1836.

(12) Samouilov, A.; Efimova, O. V.; Bobko, A. A.; Sun, Z.; Petryakov, S.; Eubank, T. D.; Trofimov, D. G.; Kirilyuk, I. A.; Grigor'ev, I. A.; Takahashi, W.; Zweier, J. L.; Khramtsov, V. V. In vivo proton−electron double-resonance imaging of extracellular tumor pH using an advanced nitroxide probe. Anal. Chem. **2014**, 86, 1045−1052.

(13) Gallez, B.; Mäder, K.; Swartz, H. M. Noninvasive measurement of the pH inside the gut by using pH-sensitive nitroxides. An in vivo EPR study. Magn. Reson. Med. **1996**, 36, 694–697.

(14) Sotgiu, A.; Mäder, K.; Placidi, G.; Colacicchi, S.; Ursini, C. L.; Alecci, M. pH-sensitive imaging by low-frequency EPR: a model study for biological applications. Phys. Med. Biol. **1998**, 43, 1921–1930.

(15) Foster, M. A.; Grigor'ev, I. A.; Lurie, D. J.; Khramtsov, V. V.; McCallum, S.; Panagiotelis, I.; Hutchison, J. M. S.; Koptioug, A.; Nicholson, I. In vivo detection of a pH-sensitive nitroxide in the rat stomach by low-field ESR-based techniques. Magn. Reson. Med. **2003**, 49, 558–567.

(16) Khramtsov, V. V.; Grigor'ev, I. A.; Foster, M. A.; Lurie, D. J. In vitro and in vivo measurement of pH and thiols by EPR-based techniques. Antioxid. Redox Signal. **2004**, 6, 667–676.

(17) Marchand, V.; Leveque, P.; Driesschaert, B.; Marchand-Brynaert, J.; Gallez, B. In vivo EPR extracellular pH-metry in tumors using a triphosphonated trityl radical. Magn. Reson. Med. **2016**, 77, 2438–2443.

(18) Bobko, A. A.; Eubank, T. D.; Driesschaert, B.; Dhimitruka, I.; Evans, J.; Mohammad, R.; Tchekneva, E. E.; Dikov, M. M.; Khramtsov, V. V. Interstitial inorganic phosphate as a tumor microenvironment marker for tumor progression. Sci. Rep. **2017**, 7, 41233.

(19) Sato-Akaba, H.; Fujii, H.; Hirata, H. Improvement of temporal resolution for three-dimensional continuous-wave electron paramagnetic resonance imaging. Rev. Sci. Instrum. **2008**, 79, 123701.

(20) Sato-Akaba, H.; Kuwahara, Y.; Fujii, H.; Hirata, H. Half-life mapping of nitroxyl radicals with three-dimensional electron paramagnetic resonance imaging at an interval of 3.6 seconds. Anal. Chem. **2009**, 81, 7501–7506.

(21) Komarov, D. A.; Hirata, H. Fast backprojection-based reconstruction of spectral-spatial EPR images from projections with the constant sweep of a magnetic field. J. Magn. Reson. **2017**, 281, 44–50.

(22) Kawada, Y.; Hirata, H.; Fujii, H. Use of multi-coil parallel-gap resonators for co-registration EPR/NMR imaging. J. Magn. Reson. **2007**, 184, 29–38.

(23) Goodwin, J.; Yachi, K.; Nagane, M.; Yasui, H.; Miyake, Y.; Inanami, O.; Bobko, A. A.; Khramtsov, V. V.; Hirata, H. In vivo tumour extracellular pH monitoring using electron paramagnetic resonance: the effect of X-ray irradiation. NMR Biomed. **2014**, 27, 453–458.

(24) Snedecor, G. W.; Cochran, W. G. Statistical Methods, 8th edition; Iowa State University Press: Ames, 1989; pp 83–106.

(25) Komarov, D. A.; Dhimitruka, I.; Kirilyuk, I. A.; Trofimiov, D. G.; Grigor'ev, I. A.; Zweier, J. L.; Khramtsov, V. V. Electron paramagnetic resonance monitoring of ischemia-induced myocardial oxygen depletion and acidosis in isolated rat hearts using soluble paramagnetic probes. Magn. Reson. Med. **2012**, 68, 649–655.

(26) Gorodetsky, A. A.; Kirilyuk, I. A.; Khramtsov, V. V.; Komarov, D. A. Functional electron paramagnetic resonance imaging of ischemic rat heart: Monitoring of tissue oxygenation and pH. Magn. Reson. Med. **2016**, 76, 350–358.

(27) Wojtkowiak, J. W.; Cornnell, H. C.; Matsumoto, S.; Saito, K.; Takakusagi, Y.; Dutta, P.; Kim, M.; Zhang, X.; Leos, R.; Bailey, K. M.; Martinez, G.; Lloyd, M. C.; Weber, C.; Mitchell, J. B.; Lynch, R. M.; Baker, A. F.; Gatenby, R. A.; Rejniak, K. A.; Hart, C.; Krishna, M. C.; Gillies, R. J. Pyruvate sensitizes pancreatic tumors to hypoxia-activated prodrug TH-302. Cancer Metab. **2015**, 3, 2.

(28) Suit, H. D.; Suchato, C. Hyperbaric oxygen and radiotherapy of a fibrosarcoma and of a squamous-cell carcinoma of C3H mice. Radiology **1967**, 89, 713–719.

(29) Matsumoto S, Hyodo, F.; Subramanian, S.; Devasahayam, N.; Munasinghe, J.; Hyodo, E.; Gadisetti, C.; Cook, J. A.; Mitchell, J. B.; Krishna, M. C. Low-field paramagnetic resonance imaging of tumor oxygenation and glycolytic activity in mice. J. Clin. Invest. **2008**, 118, 1965–1973.
(30) Provent, P.; Benito, M.; Hiba, B.; Farion, R.; López-Larrubia, P.; Ballesteros, P.; Rémy, C.; Segebarth, C.; Cerdán, S.; Coles, J. A.; García-Martín, M. L. Serial in vivo spectroscopic nuclear magnetic resonance imaging of lactate and extracellular pH in rat gliomas shows redistribution of protons away from sites of glycolysis. Cancer Res. **2007**, 67, 7638–7645.

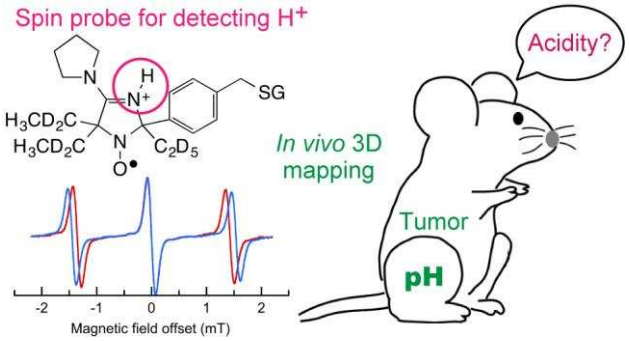
Spin probe for detecting H+
SG
H3CD2C
H3CD2C
C2D5
-2
-1
0
1
2
Magnetic field offset (mT)
In vivo 3D mapping
Acidity?
Tumor
pH